X-Ray Absorption Spectroscopy (XAS) Combined with Other Spectroscopic Techniques

33

Giovanni Agostini and Ana Iglesias-Juez

Contents

Abstract

The aim of this chapter is to show some experimental cases of X-ray absorption (XAS) application to the field of catalysis where its use had a special relevance to unravel key aspects of the catalyst preparation, characterization and reaction monitoring.

Another chapter of this book describes in detail the theoretical foundations and main applications of XAS. Therefore here, we will focus on showing the added value of combining this powerful tool with other characterization techniques, specifically with infrared Fourier transform (IR-FT) absorption spectroscopy, to investigate catalysts and catalytic reactions under real reaction conditions. The complementary association with IR spectroscopy yields highly relevant added chemical information to the electronic and structural insights provided by XAS.

In the last years, distinctive setups have been designed to combine several in situ methods. We will provide a brief revision of setups equipped with combined XAS with IR spectroscopy for in situ/*operando* studies. Three selected examples will be showed to demonstrate the great benefits of multi-technique in situ/*operando* approaches to provide essential outcomes.

Keywords

X-ray absorption · XAS · XANES · EXAFS · DRIFTS · FTIR · XRD · Multi-technique Characterization · *Operando* · In situ · Setups · Instrumentation · Electronic and structural properties

33.1 Introduction

Rational catalyst design based on understanding catalytic reactions from a fundamental point is necessary to enable the new creation of more efficient and sustainable catalytic materials and processes.

To obtain such detailed information is necessary to understand the interaction between reactants and catalysts, to discriminate between spectator species and species actively involved in the catalytic reaction, to recognize the active sites, and to correlate catalyst performance with their local structure and electronic properties. This entails that multifaceted information is required.

However, each spectroscopic technique has its own limitations and sensitivity, and therefore, the employment of a single technique will not provide all necessary chemical and physical information about the catalytic system. It becomes essential an intelligent combination of two or more spectroscopic techniques in order to provide complementary information and must be carried out simultaneously to guarantee absolutely identical environment (e.g., temperature, gasses, pressure, etc.) and ensure the comparability of results.

Furthermore, this multi-technique characterization approach must be coupled simultaneously with measurement of catalytic activity and selectivity in order to critically assess

G. Agostini
Experimental Division – NOTOS, ALBA Synchrotron, Barcelona, Spain
e-mail: gagostini@cells.es; gio.agostini@gmail.com

A. Iglesias-Juez (✉)
Catálisis Aplicada, Instituto de Catálisis y Petroleoquímica CSIC, Madrid, Spain
e-mail: ana.iglesias@icp.csic.es

I. E. Wachs, M. A. Bañares (eds.), *Springer Handbook of Advanced Catalyst Characterization*, Springer Handbooks,
https://doi.org/10.1007/978-3-031-07125-6_33

the structure-activity relationships, thereby the study of catalysts under working conditions where chemical and structural transformation takes place. This is considered an *operando* methodology [1].

But it is not only important to understand what happens during reaction conditions. It is also crucial the control on preparation of new materials and complex structures, with new electronic and structural properties that enable the improvement of the abovementioned catalytic processes. For this reason, in order to establish a complete concept scheme which would allow to predict and control the behavior of nanostructures and real systems, it is necessary to study the different physicochemical phenomena that catalyst undergoes during its whole life, i.e., formation and activation of the active centers, behavior under reaction conditions, deactivation processes, regeneration modes, etc.

This type of characterization also requires temporal resolution closed to turnover numbers (measure in sub-millisecond or even sub-nanosecond region) in combination with fast online product analysis to allow transient kinetic experiments and the use of step−/pulse-response tests to differentiate spectator from active species.

Another important requirement is spatial resolution to obtain insight not only at the macroscopic level but also at the meso- and microscale, to obtain knowledge on the distribution of the active species inside the reactor, in monoliths or extrudates (real conditions for their industrial application) or in the porous structure of the support material, and finally at the nanoscopic level to visualize the active centers and the spectator species [2].

Therefore, it is required to build cells that are simultaneously a catalytic reactor and a spectroscopic cell for various techniques and that comply with all the aforementioned requirements, which implies a great challenge in the design of in situ cells, since the optimal conditions for performing spectroscopy and catalytic measurements are not identical and sometimes are contradictory.

Scientists have tried to smartly combine different techniques to maximize the information obtained from the catalyst and, consequently, to obtain a more detailed view of the global system. Of particular interest in the field of heterogeneous catalysis is the combination of "bulk" techniques (e.g., XRD, EXAFS, XANES) and surface-sensitive techniques (e.g., IR, Raman) together with the measurement of the catalytic activity (mass spectrometry, chromatography, etc.) [3]. X-ray absorption spectroscopy (XAS) has been extensively used for in situ and *operando* studies since it is capable to yield information on local and electronic structure on the absorbing elements [4]. Since the first experiment performed by Couves (1991), coupling XAS and XRD (X-ray diffraction) [5], different cells and experimental setups have been constructed for in situ or *operando* investigations joining XAS with complementary techniques [6–9]. Availability of fiber-optical systems offers the possibility to simultaneously use both Raman and UV-visible with XAS by focusing from the outside of a quartz reactor onto the catalyst bed in a very versatile way [3e–f, 7, 10]. In another chapter of this book, some descriptive examples of these combinations are also presented.

Here, we will try to show some examples of the XAS technique where its proper combination with diffuse reflectance infrared Fourier transform spectroscopy (DRIFTS) (and also DRIFTS/XRD) and MS techniques provided a complementary vision that allowed obtaining information regarding the reaction mechanism and the activation process of the active centers. This is a powerful combination since it covers an important range of properties and phenomena of interest in the solid-gas phase from the heterogeneous catalytic life cycle [11]. Moreover, it allows at the same time:

- Bulk characterization of the active centers: structural, morphological, and size characteristics together with electronic properties and their behavior at local order by XANES (X-ray absorption near-edge structure) and EXAFS (extended X-ray absorption fine structure), while XRD provides long-range structural information.
- Catalyst surface characterization along with identification of adsorbed species and their evolution by DRIFTS.
- Quantification and evolution of reaction products by MS.

Several configurations have been designed for this purpose in the last years. As mentioned above, the combination of different spectroscopies for *operando* investigation implies to accomplish several requirements often in contrast with each other. In this case, the possibilities to probe the sample by different wavelengths (X-ray/IR), using high temperature, high pressure, small dead volume, etc., are some of them. Taking into account these requisites, the setups have adopted different design solutions by either adapting commercial cells or designing their own device. We will briefly present a description of their evolution. Among all of them, two recent solutions will be presented below due to their flexibility and general purpose that provide the greatest potential and versatility to date.

- Newton and co-workers carried out a pioneering work [12] devoted to catalysis at ID24 beamline of the European Synchrotron Radiation Facility (ESRF), using a custom-built DRIFTS cell modifying the setup proposed by McDougall [13]. The design of a flat top allowed minimizing the dead volume of the cell providing a fast response to gas switchings. However, temperature was limited up to 400 °C, and the cell presented a gas feed bypass in the catalytic bed. To solve this issue, a commercial cell from SpectraTech was modified [14a], but the problem was not completely sorted out, and on the

contrary, dead volume increased compared to the previous cell.

- A comparable setting was developed at Brookhaven National Laboratory and mounted at X18 beamline [14b] using a modified Praying Mantis™ diffuse reflection accessory with an attached da Vinci arm and a Harrick cell that was placed in the internal sample chamber of the IR spectrometer. This system worked up to some higher temperatures (500 °C) but still at ambient pressure. Another similar attempt was also constructed at Argonne National Laboratory with the added advantage of enabling both transmission and fluorescence XAS measurements [14c, d].
- These previous designs used samples in powder form. Bando et al. [15a, b] employed a relatively simple cell where a pelleted sample was placed in the center of a cross-like chamber allowing to measure both X-ray and IR in transmission geometries. The maximum allowed temperature and pressure were 530 °C and 3 bars, respectively, but with both large dead volume and bed bypass problems.
- Later, Chiarello proposed a different design [15c]. This new cell had a single window, in direct contact with the sample, for both X-rays and IR radiation. This allowed reducing the dead volume and working as a plug flow reactor. This permits the rapid exchange of gases necessary to carry out transient experiments. However, this design presents some disadvantages: it is necessary to drill a small hole (0.5 mm in diameter) in the CaF_2 IR window for XAS spectra acquisition and to seal it with a glue with a high thermal stability based on carbon. The cell was used up to 500 °C, at ambient pressure, and it was also tested combining XRD and IR at the same time [15d].
- Recently, Agostini et al. [16] presented a new design at ID24 (ESRF) to perform *operando* measurements for solid-gas reaction catalysts, recovering the idea proposed by McDougall [13] but overcoming some limitations of the previous mentioned versions. In particular, the cell design was optimized to minimize dead volume, prevent any bypass of the sample by gasses, and work at high temperatures (up to 600 °C) and under pressure (7 bars) in transmission mode. It allows to optimize radiation windows for both IR and X-rays (using different window materials and thickness), and it houses the sample in powder form. These issues are essential to enable testing different experimental conditions (e.g., variety of metal loadings and supports, wide X-ray energy range, etc.). In order to expand the range of possibilities, newly design improvements allow now XAS measurements in fluorescence mode for highly dilute materials and/or heavy matrices [17]. The flat top window makes also sample surface accessible by other spectroscopies like UV-vis or Raman.
- Recently, Urakawa and co-workers proposed an innovative approach combining XAS and XRD with IR spectroscopy and using pelleted sample [18]. The flexibility of a modular IR interferometer allows to change the relative position of the IR source and the IR radiation detector, being possible to work in both transmission and diffuse-reflection configurations. Transmission mode using a pelleted material often results in higher data quality although sample preparation and handling could involve difficulties to fulfil and, at the same time, the different sample requirements for IR and XAS or XRD techniques.

33.2 Examples

33.2.1 Study Case 1: XAS Combined with DRIFTS and MS

In the field of heterogeneous catalysis, Pt-based metallic systems are of great relevance since they are used in numerous industrial processes due to their excellent reactivity. For example, Pt-catalysts present unique properties for hydrogen activation, being widely used in processes involving hydrogenation reactions (e.g., of numerous organic substrates), since they allow operating in milder conditions guaranteeing high conversion and selectivity. In these processes, the homolytic dissociation of the hydrogen molecule is the crucial step which leads to the formation of different metal hydride species on the platinum surface. These species directly participate in the hydrogenation route, and their type and quantity greatly depend on the operating conditions.

Therefore, obtaining a realistic model of hydrogen adsorption on Pt nanoparticles, depending on the reaction conditions, is highly relevant industrially, since it will allow the correct choice of operating conditions and/or the design of higher performance catalysts.

So far, there are lots of experimental and theoretical studies [19] on supported Pt nanoparticles subjected to hydrogenation conditions that give evidence that H_2 induces electronic and morphological reconstructions of Pt sites depending on a variety of parameters: nanoparticle support, conditions of pressure and temperature, reactant composition, and hydrogen coverage.

Nevertheless, it continues a topic of discussion the nature of those Pt centers involved in the hydrogen adsorption, the formed hydrides, and their relative concentration and reactivity under different reaction conditions [20]. Therefore, to understand and improve hydrogenation catalysis, it is necessary an entire description of all surface Pt-hydride species and their dynamic performance under different operating conditions.

In the example presented here [21], the authors have tried to shed light on the problem by using a multi-technique approach to analyze a Pt industrial catalyst (5 wt. % Pt/Al_2O_3) under different hydrogenation/dehydrogenation conditions. They designed a series of *operando* synchronous XAS/DRIFTS/MS experiments to investigate electronic and structural properties of Pt-hydrides and the modifications that take place under different reaction conditions at the Pt nanoparticles. The experiments were performed at BM23 beamline of ESRF, France, using the setup presented in Fig. 33.1. They have also combined these results with inelastic neutron scattering (INS) and high-resolution transmission electron microscopy (HR-TEM) to obtain the whole picture.

The catalyst presents small Pt nanoparticles with an average size of 1.4 nm, with almost spherical shape and distributed homogeneously on the support.

Operando DRIFTS allowed to monitor linear Pt-hydride formation during H_2 treatment and their subsequent evolution during the following dehydrogenation step. However, IR absorption bands related to n-fold coordinated Pt-hydrides (appearing below 1000 cm^{-1}) could not be detected in this case due to the presence, in that region, of intense bands ascribed to the alumina framework vibrational modes that saturate the signal of the detector. Therefore, it was necessary to complement with INS measurements to obtain a complete identification of the different types of Pt-hydrides. INS results disclosed the presence of fluctuating n-fold (bridged, hollow and fourfold) coordinated Pt-H species, even in catalyst with low Pt loading.

In the DRIFTS spectra presented in Fig. 33.2, four absorption bands are detectable at: 2115, 2041, ~1990, and ~1740 cm^{-1}, marked as I, II, III, and IV, respectively. The type I band is ascribed to a soft adsorbed linear hydride, whereas the II and III bands are attributed to stronger linearly adsorbed Pt-hydrides that differ from each other on the environment around the hydride (it depends on the H_2 coverage degree). Band IV is related to adsorbed species at the interface between the support and Pt nanoparticles. Along the reduction step, these bands grew gradually in intensity until reaching a steady state (spectrum 1 in Fig. 33.2c).

The combined results showed that when hydrogen coverage was maximum (point 1 in Fig. 33.2b), Pt particles were covered by linearly adsorbed species (type I hydride) and n-fold coordinated hydrides (INS detected). When hydrogen coverage decreased, the linear hydrides (IR band I) rapidly disappeared, while n-fold coordinated hydrides (INS detected) slowly evolved into linear species, causing the transient intensity increase of bands II and III. Along the dehydrogenation process, a relative intensity change between bands II and III was also detected, and band III prevails at longer times. Band IV remains almost unchanged along the time until the end of the process when quickly disappeared as bands II and III.

On another hand, XAS results point to significant changes in the Pt nanoparticles during the dehydrogenation process. Pt L_3-edge XANES spectra (Fig. 33.3a) present modifications in the intensity and shape of the white line, indicative of electronic effects induced by the adsorbate [19a, 22]; thus it,

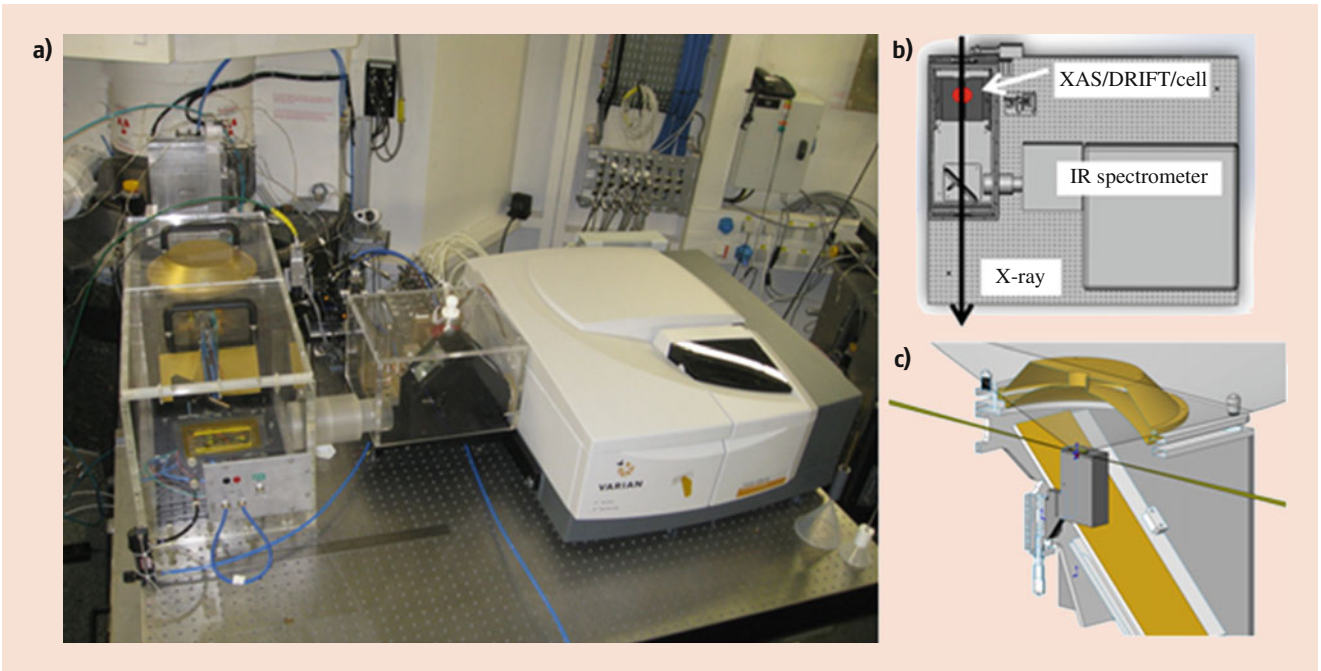

Fig. 33.1 (**a**) ID24-mounted XAS/DRIFTS/MS configuration, (**b**) mounting scheme, and (**c**) schematic drawing of the DRIFTS cell mounted inside the reflectance sphere

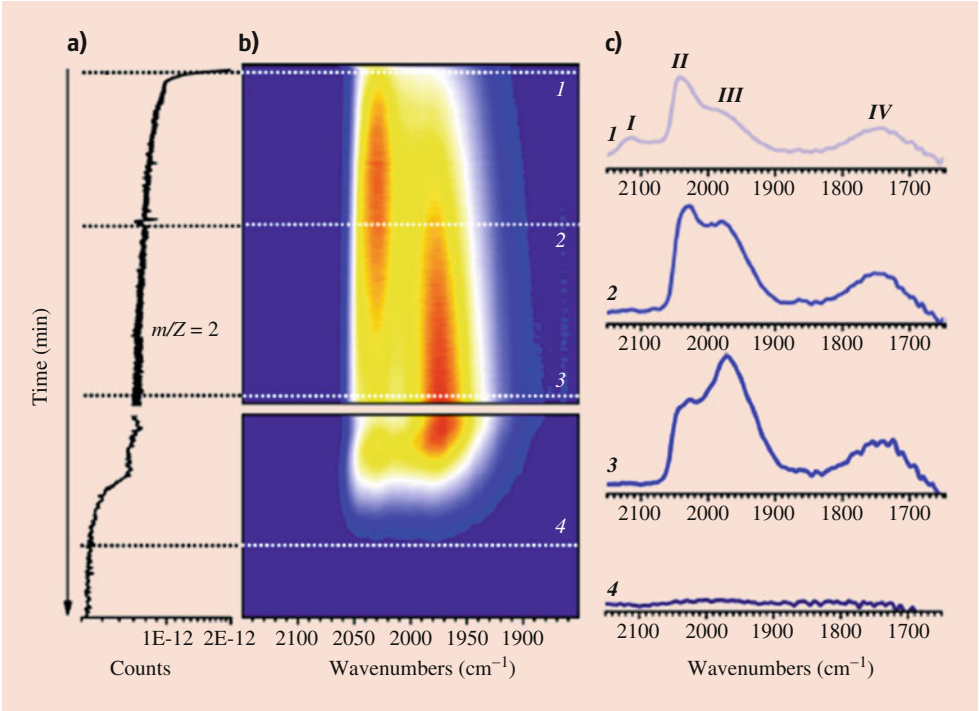

Fig. 33.2 Part (**a**): evolution of the signal corresponding to H_2 ($m/Z = 2$) as detected by the mass spectrometer placed at the outlet of the reaction cell. Part (**b**): 2D map showing the evolution of the DRIFT spectra as a function of time for the Pt/Al_2O_3 catalyst during dehydrogenation in He flow (20 mL/min) at 120 °C, for the *operando* DRIFT/XAS/MS experiment. The reduction step preceding the dehydrogenation was accomplished in the presence of 10 mol % H_2 in He. The intensity increases from blue to red. Part (**c**): four FT-IR spectra selected at specific times (1, 2, 3, and 4 in the 2D map shown in Part **b**). The spectra are shown after subtraction of the spectrum of the catalyst before reduction, in the 2150–1850 cm^{-1} range. (Reproduced from Ref. [21] with permission from the American Chemical Society)

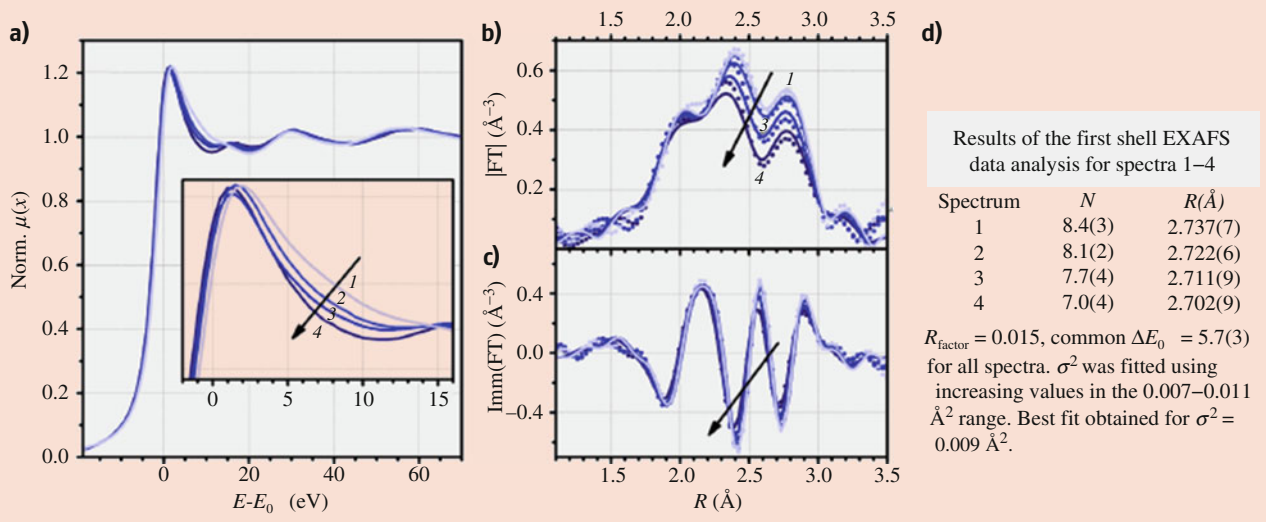

Fig. 33.3 Part (**a**): evolution of the normalized Pt L_3-edge XANES spectra of the Pt/Al_2O_3 catalyst during dehydrogenation in He flow (20 mL/ min) at 120 °C, collected during the *operando* DRIFT/XAS/MS experiment (E_0 = 11,564 eV). The inset shows a magnification of the white-line region. Part (**b**): modulus of the Fourier transforms of the k^2-weighted EXAFS signals collected along with the XANES spectra reported in Part **a**. The experimental signals (dotted) are overlapped to the first shell fits (full line). Part (**c**): the same as part **b**, for the imaginary part of the Fourier transforms. Spectra 1–4 closely correspond to the DRIFT spectra 1–4 in Fig. 33.1. Part (**d**): EXAFS data analysis results. (Reproduced – adapted from Ref. [21] with permission from the American Chemical Society)

chemisorbed hydrogen, withdraws electrons from the platinum atoms and leads to a reduced electron density in those centers. Furthermore, in the EXAFS data (Fig. 33.3b, c), a small intensity decrease of the first coordination shell in the Fourier transforms and a shift toward shorter distances were observed. A detailed data analysis (Fig. 33.3d) demonstrates that platinum nanoparticles underwent a progressive reconstruction during hydrogenation/dehydrogenation steps, showing a good agreement with theoretical calculation [23].

The combination of all the acquired data show that linear and n-fold coordinated platinum-hydrides are formed when increasing hydrogen coverage, solvating gradually the Pt clusters. At high hydrogen saturation, the platinum clusters adopt a cuboctahedral shape. A decrease in the H_2 partial pressure induces a reconstruction of the platinum particles toward a biplanar shape covered mainly by linear hydrides.

Therefore, this work is an excellent example of how a clever combination of XAS with other techniques, especially DRIFTS, allows the complete examination of what happens on the surface of the Pt nanoparticles. It is worth noting that each technique, as a single measurement, cannot provide an overview of the entire process; thus, XAS allows to follow the morphology and electronic-structural changes of the Pt nanoparticles, but it is unable to identify the surface Pt-H species directly involved in the catalysis that were distinguished by combining with DRIFTS and INS since, in turn, each of these spectroscopies only tracks a fraction of surface Pt-hydride species and cannot provide information on the shape and structure of the platinum.

Even more important for the catalysis, in this work they were able to follow the behavior of Pt-hydrides during the catalytic hydrogenation of toluene to methylcyclohexane (MCH), chosen as a model for catalytic hydrogenation of substituted benzenes, applying the same XAS//DRIFTS/MS approach described above. The DRIFTS data are showed in Fig. 33.4b, c: bands I and II immediately disappear after introducing the reactant mixture, while the intensity of band III rapidly increases, and band IV remains almost unaltered. At the same time, the MS results (Fig. 33.4a) indicate that toluene conversion starts instantaneously and MCH evolves parallel to the concomitant disappearance of the band I. Toluene conversion proceeded at a constant rate for the whole investigated time. Then, DRIFTS spectra stay constant along the reaction time. The reverse behavior is detected when toluene is removed from the reaction feed.

However, XAS data show that under these reaction conditions, Pt nanoparticles are stable and do not present any electronic or structural alteration during the reaction time as no changes in XANES (Fig. 33.5a) and EXAFS (Fig. 33.5b, c) spectra were observed.

These experiments revealed that the species directly involved in the hydrogenation of toluene are the most weakly

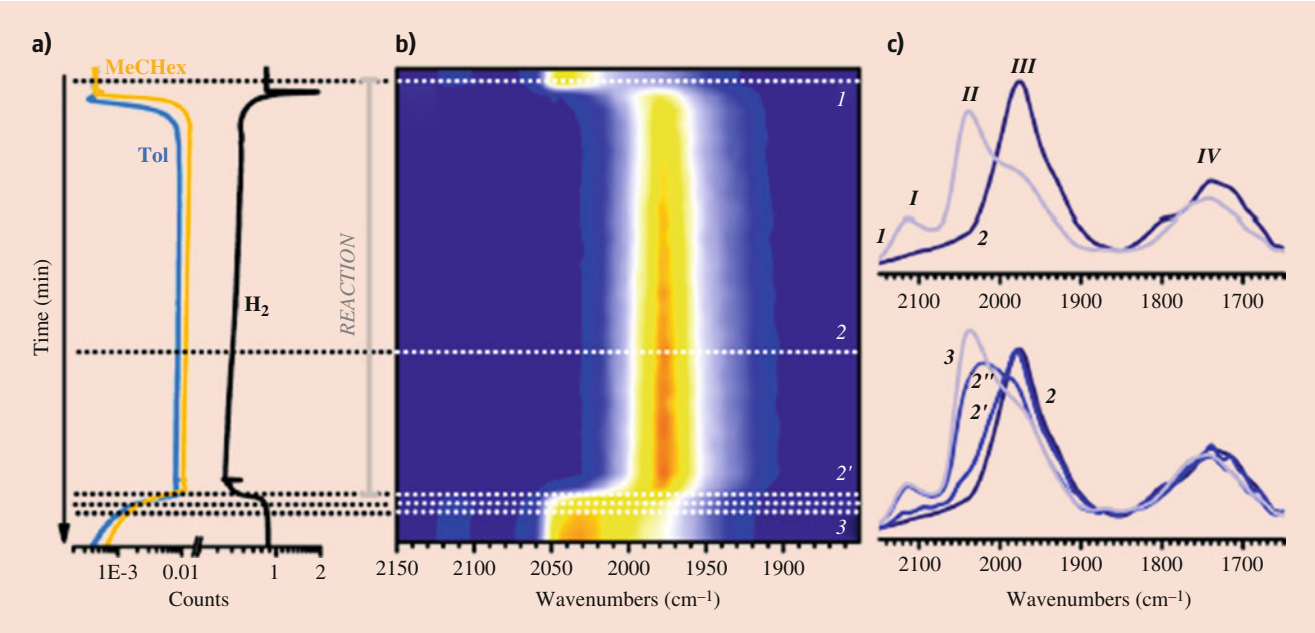

Fig. 33.4 Part (**a**): evolution of the signals corresponding to H_2 ($m/Z = 2$), toluene ($m/Z = 91$), and MCH ($m/Z = 55$), as detected by the mass spectrometer placed at the outlet of the reaction cell. Part (**b**): 2D map showing the evolution of the DRIFT spectra as a function of time for the Pt/Al_2O_3 catalyst during hydrogenation of toluene to MCH at 120 °C. The reduction step preceding the reaction was accomplished in the presence of 10 mol % H_2 in He. The intensity increases from blue to red. Part (**c**): FT-IR spectra selected at specific times as indicated in the 2D map shown in Part (**b**). Spectrum 1, before the onset of the reaction; spectrum 2, after 1 h reaction; and spectrum 3 after toluene elimination from the feedstream. The spectra are shown after subtraction of the spectrum of the catalyst before reduction, in the 2150–1850 cm^{-1} range. (Reproduced from Ref. [21] with permission from the American Chemical Society)

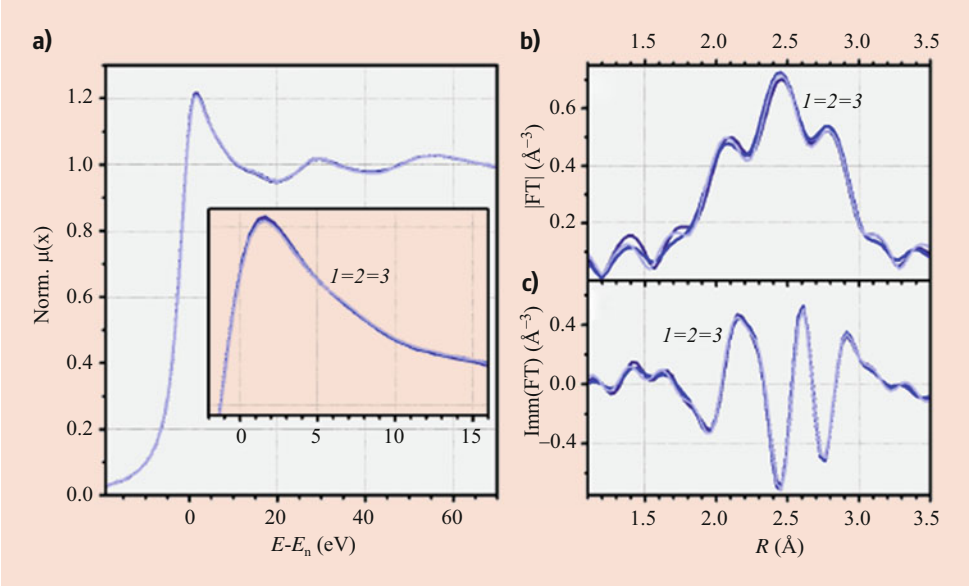

Fig. 33.5 Part (**a**): evolution of the normalized Pt L_3-edge XANES spectra of the Pt/Al_2O_3 catalyst during hydrogenation of toluene to methylcyclohexane at 120 °C, collected during the *operando* DRIFT/XAS/MS experiment (E_0 = 11,564 eV). The inset shows a magnification of the white-line region. Part (**b**): modulus of the Fourier transforms of the k^2-weighted EXAFS signals collected along with the XANES spectra reported in Part **a**. Part (**c**): the same as Part **b**, for the imaginary part of the Fourier transforms. Spectra 1–3 closely correspond to the DRIFT spectra 1–3 in Fig. 33.2 (i.e., spectrum 1 is collected before introducing toluene in the reaction feed, spectrum 2 during the toluene hydrogenation reaction, and spectrum 3 after removal of toluene from the reaction feed). (Reproduced from Ref. [21] with permission from the American Chemical Society)

adsorbed hydrides (type I species), while the other surface Pt-hydrides do not intervene but keep the Pt nanoparticles H-covered. This confers electronic and morphological stability along the reaction, avoiding the appearance of the undesirable deactivation processes, and therefore, they are also key species in the process.

33.2.2 Study Case 2: XAS Combined with DRIFTS and MS

Supported Pd nanoparticles are applied in numerous areas as biomass conversion, water gas shift, coupling transformations in organic synthesis (e.g., Suzuki-Miyaura and Mizoroki-Heck reactions), selective oxidations for fine chemical production, and pollution abatement from automobile exhaust. This noble metal displays a unique behavior in oxidation processes, and this is the key aspect that supports its use in all these catalytic applications [24].

This second example reveals the rich chemistry of palladium nanoparticles by the synchronous use of XAS/DRIFTS/MS [25]. This approach allowed to disclose a series of size-dependent phenomena in the palladium response to the dynamic conditions of reactive atmosphere. More specifically, the multi-technique study was applied to investigate Pd-based three-way catalysts (TWCs). TWCs are a widely used technology in gasoline vehicle exhausts for controlling pollutant emissions. These systems convert simultaneously three pollutants to harmless emissions – carbon monoxide (CO), hydrocarbons (HC), and nitrogen oxides (NO_x) – in the presence of water and O_2 [24c]. During typical TWC operation, the gas atmosphere oscillates around the stoichiometric point (exact balance of oxidant to reducing molecules) [24c, 26], and the active noble metal component must work under alternating oxidizing and reducing periods (ca. 1–3 Hz frequency). Therefore, Pd chemical state is one of the key factors governing the catalytic behavior. Here, the authors used different Pd/Al_2O_3 catalysts as models to investigate the nanoparticle size influence on the structural-redox-temporal response of the supported Pd particles, and what interrelated consequences has in their chemical activity.

Regarding CO oxidation, there has been an intense debate about whether the most active phase, under oscillatory conditions, is related to a surface layer of Pd oxide [27] or is a metallic phase covered with chemisorbed oxygen [28]. For this reason, they focused on the analysis of two model reactions under cycling conditions (dynamic realistic situation) for CO oxidation: with NO + O_2, constituting the two main oxidant species present in the exhaust gases, and with only NO, in order to differentiate between competitive interaction of both oxidant molecules and also shedding on the activation of two of the key reactants, CO and NO.

A series of samples with increasing palladium loading (1, 2, and 4 wt.%, labelled: 1PdA, 2PdA, and 4PdA, respectively) was prepared for a time-resolved (sub-second) study during reducing/oxidizing cycling conditions.

Figure 33.6a displays a representative behavior of the Fourier transform of the EXAFS spectra during cycling CO/NO gas mixture. The coordination numbers (CN) for the first Pd-Pd shell were obtained fixing Debye-Waller (DW) factors. The evolution of the corresponding CNs extracted from EXAFS fittings of the series of samples is shown in Fig. 33.1. In all cases, Pd metal phase responded actively to the nature of the gas mixture, showing that the CN increased under CO atmosphere and dropped to the initial value during NO exposure in a fully reversibly way. This performance was quantified by estimation of the Pd dispersion (ratio of surface atoms and total number of atoms) calculated from CNs and applying Jentys [29] procedure. Cuboctahedral particle shape and exclusive size effect (Fig. 33.6b) assumptions were considered. Particle size was estimated as ca. 1.5, 2.5, and 3.5 nm for the 1, 2, and 4PdA samples, respectively. All Pd catalysts present similar performance, but higher variations in the dispersion were observed for bigger particles, which suffer stronger morphological modification. A region displaying smooth variation was observed at the middle-end part of the CO feed. This behavior may be explained with the help of XRD collected using the same conditions and sample environment adopted in the XAS experiment. The data clearly showed a transient variation in the d-spacing of the Bragg reflections from Pd nanoparticles (Fig. 33.7): this phenomenon is associated to palladium carbide phase formation during CO gas exposure. Atomic carbon is obtained as product of "Boudouard" reaction ($2CO \rightarrow CO_{2g} + C_a$) that occurs at high-coverage CO ad-layer. C atoms were introduced at interstitial positions of the metal *fcc* structure [30]. A maximum in C-content was found for the 2PdA sample. This phase was somewhat unexpected, as it was not previously observed using stoichiometric CO-NO composition, stressing the importance of studying systems under more realistic dynamic conditions.

Complementary information was extracted by synchronous DRIFTS measurements, providing parallel analysis of the gas-solid interface, and mass spectrometry allowing to follow the global activity/selectivity. Correction of DRIFTS and MS signals under *operando* conditions was done normalizing DRIFTS and MS observables using the structural information obtained from EXAFS analysis, in order to interpret chemical activity in terms of surface Pd sites.

DRIFTS results (Fig. 33.8) displayed that the ratio between on-top (2050–2020 cm^{-1}) and bridge (1925–1900 cm^{-1}) Pd(0) carbonyls varied a long time revealing the promotion of linearly bound CO over the bridged concomitantly to the PdC_x phase formation. This suggests that the carbide phase is formed from CO dissociation and led to carbon species storage in the Pd metal. In addition, that phase was fully removed during the switch from CO to NO feeds accompanied by the formation of a large amount of NCO (2240 cm^{-1}). This study was able to show a new NCO formation route derived from withdrawal by molecular NO of atomic carbon transiently stored within the Pd nanoparticles, that is, a path where NO does not dissociate.

Thanks to the CNs extracted from EXAFS analysis, the chemical response of the Pd/Al_2O_3 systems to the gas cycling conditions was analyzed establishing a Pd size dependence of all crucial chemical steps related to gas reactant adsorption,

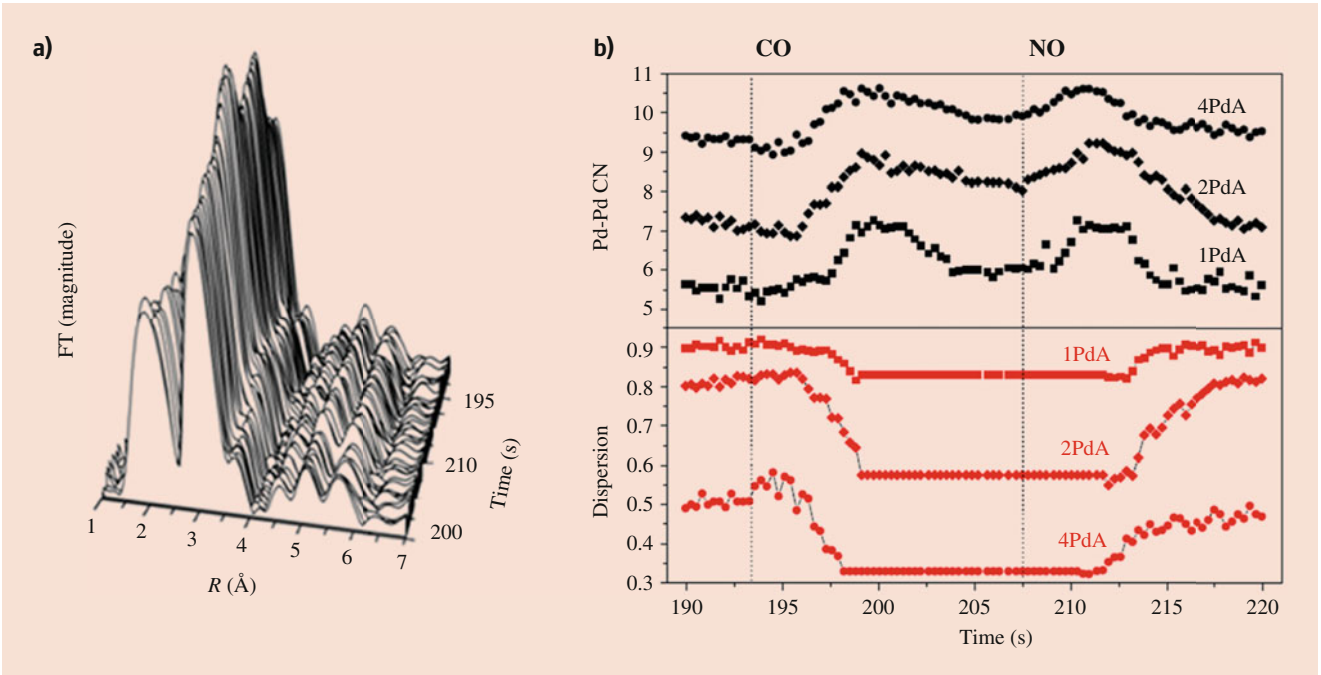

Fig. 33.6 (**a**) FT-EXAFS plots of the cycling behavior of a 2 wt.% Pd/Al_2O_3 catalyst and (**b**) Pd-Pd coordination number and dispersion of several (1, 2, 4 wt.%) Pd/Al_2O_3 catalysts in a CO/NO atmosphere. (Adapted from Ref. [25] with permission from Elsevier)

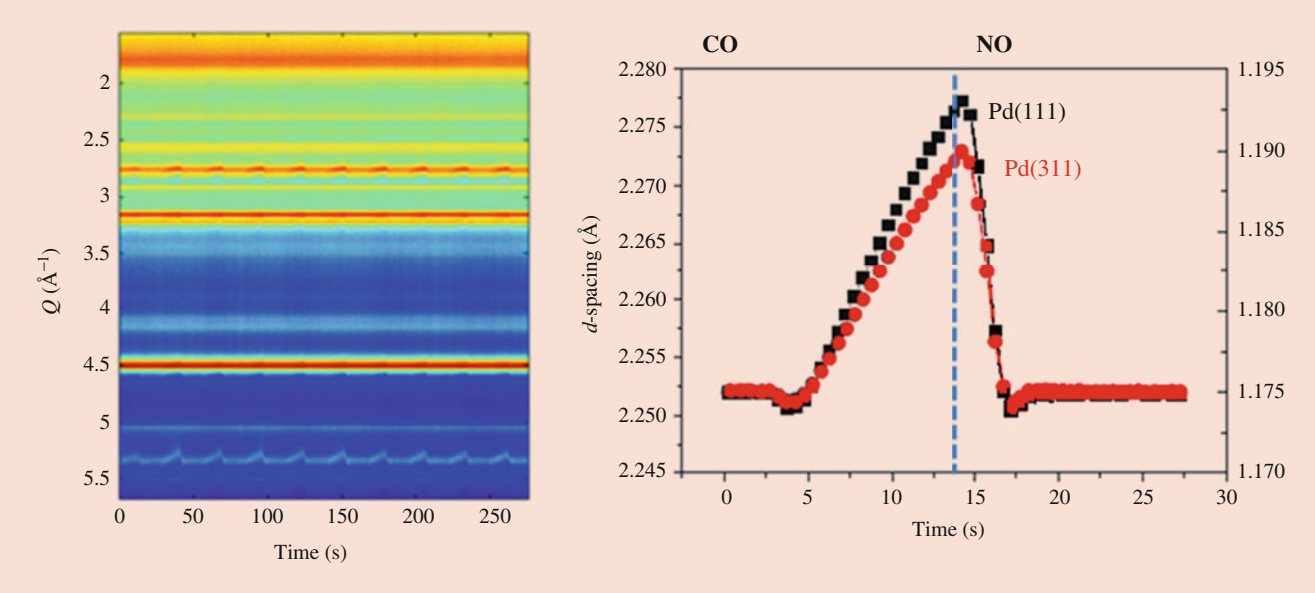

Fig. 33.7 XRD plots and variation of two Pd metal lattice planes in a CO/NO atmosphere for a 2 wt.% Pd/Al_2O_3 catalyst. (Adapted from Ref. [25] with permission from Elsevier)

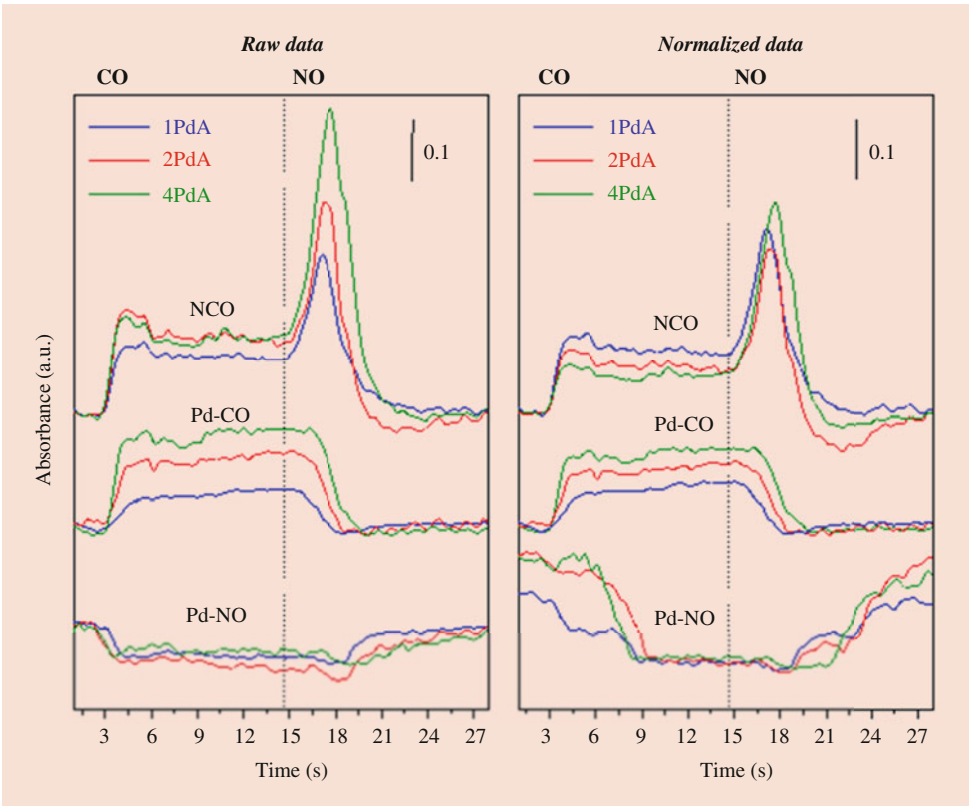

Fig. 33.8 DRIFTS band intensity plots vs. time (raw and normalized per Pd surface atom) of characteristic absorbed species during CO/NO cycling atmosphere for several (1, 2, 4 wt. %) Pd/Al_2O_3 catalysts. (Adapted from Ref. [25] with permission from Elsevier)

dissociation, and activation steps. The size effects on the adsorption pathways of reactants were scarce and only linked to NO (its adsorption was favored when increasing particle size, although above 2.5 nm it was barely affected). Regarding the evolution of products, for N_2 formation, N-N coupling was the limiting step of the reaction, and the recombination is favored with the particle size of Pd, although above 2.5 this sensitivity to size decreases. On another hand, for CO_2 production, an important size sensitivity ascribed to the CO desorption step was observed: desorption

path is favored as Pd particle size decreases. Therefore, Pd particle size growth was detrimental for CO_2 formation. This finding was contrary to the assumptions made from measurements under non-cycling conditions.

When both oxidant reactants were presented ($NO+O_2$) [25a] during gas cycling conditions, the Pd chemical response was different and more complex. Factor analysis (FA) of the XANES spectra acquired during time-resolved cycling allowed to determine the number of Pd chemical species and their evolution along the reaction. XANES spectra corresponding to the pure chemical species and their concentration profiles are presented in Fig. 33.9. As for CO/NO experiment, two species, Pd(0) and Pd(II), were observed during cycling. But for Pd particles smaller than 3 nm, the presence of a third species Pd(I) was detected. It corresponds to a surface oxide layer with a characteristic electronic structure, which preserves a certain metallic character. The appearance of this species in the 2PdA case delayed Pd(0) formation during CO exposure relative to the 4PdA sample (EXAFS and XRD results also confirmed this behavior). Interestingly, the previously detected Pd carbide phase (PdC_x) during CO/NO cycling case was completely suppressed in the present conditions.

The differences in Pd oxidation state at surface and bulk were completed with synchronous DRIFTS results. The weak nature of Pd(I) carbonyls avoids their detection by DRIFTS under the current conditions (the application of FA to XANES data was key to identify this species). DRIFTS spectra were dominated by on-top and bridge Pd(0) carbonyls, NCO on alumina, and CO_2 gas contributions. 2PdA also displayed a signal characteristic of a Pd(0) nitrosyl (ca. 1765 cm^{-1}) species [1, 2]. NCO species was greatly reduced with respect to the CO/NO case. The presence of oxygen-adsorbed species during NO + O_2 atmosphere effectively curtails the formation of PdC_x species, and therefore, the alternative pathway for NCO formation (previously revealed) is inhibited in these conditions.

The biggest finding was that both Pd(I) and Pd(0) species can exist at palladium surface, but their presence is highly dependent on the Pd nanoparticle size. Both species are active centers for CO elimination, but the results suggested Pd(I) species present a higher activity and can be considered the "active" surface Pd oxide layers for CO conversion. Above 3 nm diameter size, the instability of the Pd(I) species may be associated to a stronger interaction with the oxygen molecule relative to particles with smaller size, and only Pd (0) was detected as the active species for CO elimination at the surface of palladium nanoparticles. These results pointed the importance of adjusting and maintaining the Pd nanoparticles in a certain size to achieve more efficient catalysts in the oxidation of CO under real operating conditions.

This example shows the important role of redox chemistry processes in controlling catalytic activity and discloses a significantly richer chemistry than may have been previously assumed, such as size-dependent phenomena. In particular, CO oxidation can involve a series of unexpected steps. The study unveiled the role of Pd carbide phase, resulting from CO dissociation, under CO/NO cycling conditions. It also showed a novel route for NCO formation. When NO and O_2 compete together, surface oxygen adsorption inhibits PdC_x formation. How strong the interaction of the oxygen molecules with palladium nanoparticles is size-dependent and determines the redox surface state. Pd(I) species were demonstrated to be the active centers for CO oxidation, and also

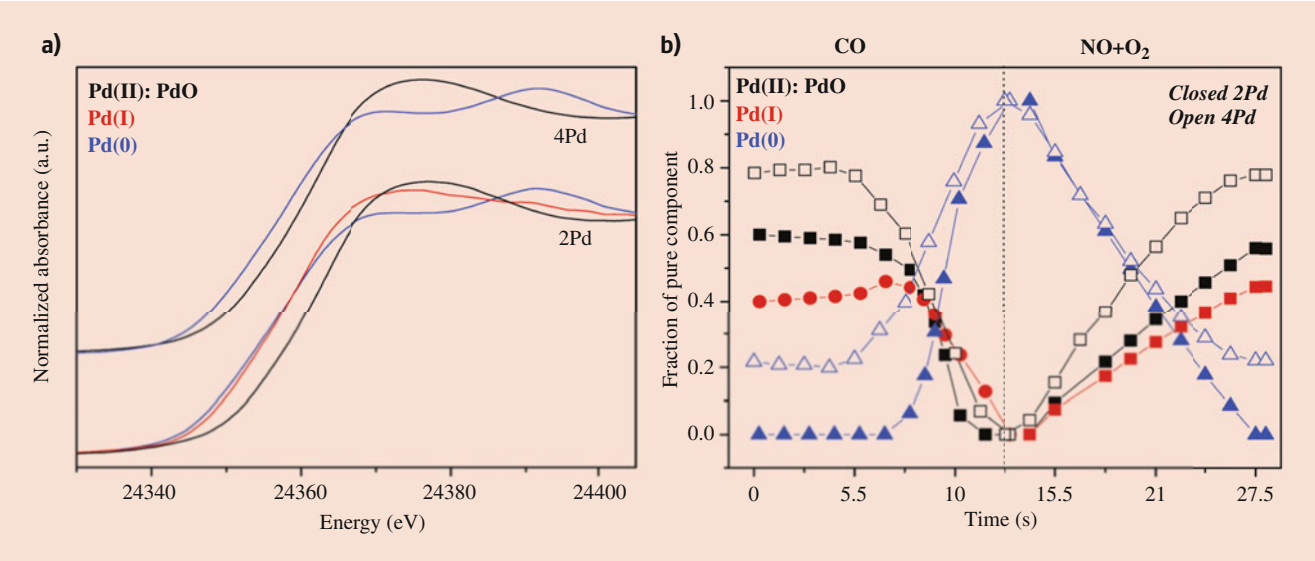

Fig. 33.9 XANES spectra (**a**) and concentration profiles (**b**) corresponding to pure chemical species (obtained by factor analysis) present during a single CO/($NO+O_2$) cycling treatment at 673 K. (Reproduced from Ref. [25] with permission from the American Chemical Society)

their presence depends on Pd particle size. The experiments uncover the size dependency of the Pd chemical activity when dynamic redox situation. Combined *operando* use of XAS/DRIFTS/MS revealed such physical-chemical performance, valuable for practical use of Pd-TWC systems for pollutant abatement.

33.2.3 Study Case 3: XAS Combined with Transmission FT-IR and X-Ray Diffraction

Metal-organic frameworks (MOFs) have burst onto the catalysis landscape as a special type of materials due to several special features: organic-inorganic hybrid nature, modular assembly, a high surface area, crystalline, and readily functionalized pore structures.

MOFs can present intrinsic catalytic activity or can be used as hosts for the incorporation of metal nanoparticles or other catalytic moieties. They can trigger photo- and electrocatalytic reactions by using their optoelectronic properties and ligand-to-metal charge transfer or can be used as catalyst precursors via controlled decomposition. The possibility of targeted assembly from rational preselected molecular building blocks or post-synthetic modification of the MOF structure etc. offers a lot of potential to construct new functional orientated porous materials. MOFs are of interest for different applications: storage of gases (as H_2 and CO_2); gas purification; gas separation; in catalysis, as conducting solids; and as super-capacitors [31, 32].

In this example [18], simultaneous measurements of XAS, transmission FT-IR, and XRD were combined to study the behavior of metal-organic frameworks (MOFs) during thermal treatment. This is an activation protocol generally used with these systems, and, therefore, getting insights on the formation of the active sites for catalytic reaction is of special interest to understand the functionality of these materials and visualize their potential applications.

In this case, working in transmission configuration with a pellet form has advantages in terms of signal quality, although it could involve difficulty in sample preparation and handling. Here, the authors used a pellet formed via a two-step process: firstly a NaCl disc is prepared using high pressure, and then a small portion of the sample is deposited on the top using low pressure [18]. In this way, the amount of sample can be optimized for being used in transmission mode for XAS and IR. The material used as support disc must meet the transparency requirement for both X-ray and IR radiation in the measurement range, and sometimes fulfilling this demand can be tricky. In addition, XAS and IR spectroscopies were also combined simultaneously with X-ray diffraction providing more complete chemical, physical, geometric, and electronic information.

These multi-probe experiments combining XAS/FTIR/XRD were performed at BM31 (the Swiss-Norwegian Beamlines, SNBL) of the ESRF, France, using the setup presented in Fig. 33.10.

The studied material, Zr-BTC, is a Zr-based metal-organic framework with a structure known as MOF-808 [33]. This structure is correlated to that of zirconium terephthalate UiO-66, the most known Zr-based MOF, which shows outstanding thermal stability (up to 550 °C) as well as a good chemical stability in organic solvents and water [34]. For MOF-808, Zr-BTC is built up from zirconium oxide octahedral blocks (secondary building units with zirconium ions disposed in octahedrons, called Zr6-SBU), connected by 12 bridging carboxylates: 6 BTC (benzene-1,3,5-tricarboxylate) ligands and 6 acetates anions [33]. This type of MOFs presents remarkable properties for water absorption and adsorption [33], and initially, the sample accommodates in its porous structure a large H_2O quantity (~10 wt.% estimated from TGA analysis).

During the thermal treatment from room temperature (RT) to 150 °C under He flow and then in isothermal conditions at the same temperature, the sample was in situ

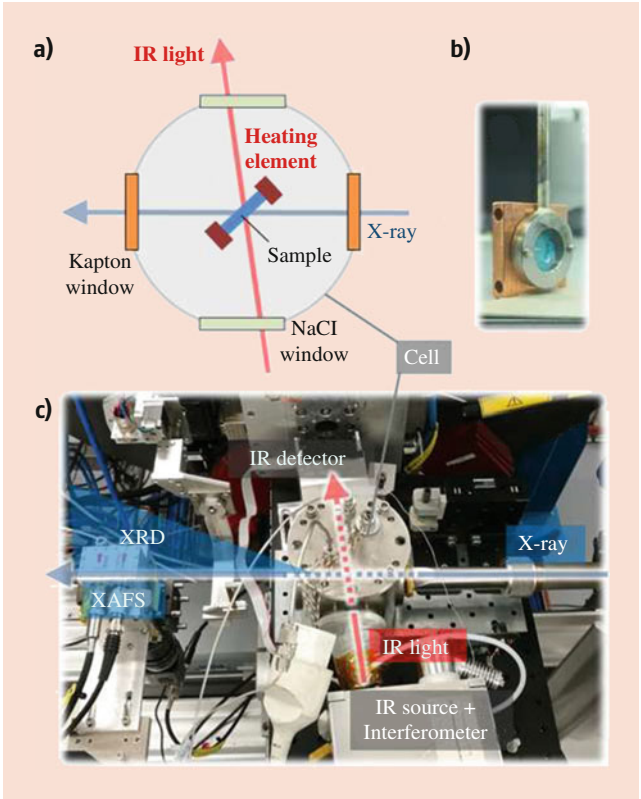

Fig. 33.10 (**a**) Schematic drawing of the cell (top view) and IR light and X-ray optical paths to perform the simultaneous XAS-XRD-IR measurements. (**b**) Pellet sample holder; heating cartridges are inserted in the holes. (**c**) Picture of the XAS- XRD-IR. (Reproduced from Ref. [18] with permission from John Wiley and Sons)

characterized by using combined XAS/FTIR/XRD to gain geometrical, electronic, and chemical information of the Zr-BTC.

Figure 33.11 summarizes the structural and electronic XRD and XAS results on the Zr-BTC during the thermal treatment. The Zr K-edge XANES spectra (Fig. 33.11a) show the intensity of the white-line decreases, while the absorption edge shifts to lower energies upon the treatment, implying a partial reduction of the Zr centers with a decrease in the coordination number. On the other hand, the structural information gained by EXAFS reflects a big change in the Zr near local environment (Fig. 33.11b). In the FT of the EXAFS signal, the initial two features at 1.8 and 3.3 Å decreased with a concomitant increase of the peaks at 1.6 and 2.8 Å. These two peaks are ascribed to Zr-O and Zr-Zr scattering paths, respectively. The first oxygen coordination sphere (EXAFS refining showed different independent Zr-O distances) decreased from a total number of 8 to a smaller value. This means that the cluster symmetry is reduced and the nature of the Zr6 SBU unit changes from the initial synthesized form to the dehydrated material [35]. Similar profiles of XANES and FT-EXAFS spectra have been also observed for another related Zr-MOF [35, 36]. Initially, the Zr6 SBU node in the Zr-BTC presents six edges bridged by the linker-bound carboxylates (BTC as threefold symmetric linkers), with the remaining six edges occupied by mono-carboxylates (acetate linkers). The structural complexity makes difficult to interpret the observed changes, but the detailed analysis of the EXAFS data suggests the changes are consistent with the removal of the acetate ligands, which was firmly proven by the complementary information from IR shown later. This causes the readjustment of the Zr coordination environment by decreasing the Zr-Zr atomic distances. Therefore, the thermal treatment causes the release of ligands which induces a chemical transformation near the Zr atoms accompanied by a partial change in their electronic structure.

XRD results (Fig. 33.11c) showed only slight changes in both the position and the intensity of some of the reflections, which could indicate some alteration of the electron density in the pores, in correlation with the reduction of the unit cell volume detected by Rietveld refinement analysis.

Therefore, all these findings show that the thermal treatment did not alter the framework structure, but it did caused modifications of the Zr6-SBU chemical and structural environment.

As previously mentioned, the complementary information provided by the simultaneous acquisition of IR spectra allowed to validate the conclusions drawn from the EXAFS analysis and obtain chemical information on the activation process. Figure 33.12 summarizes the IR data along the

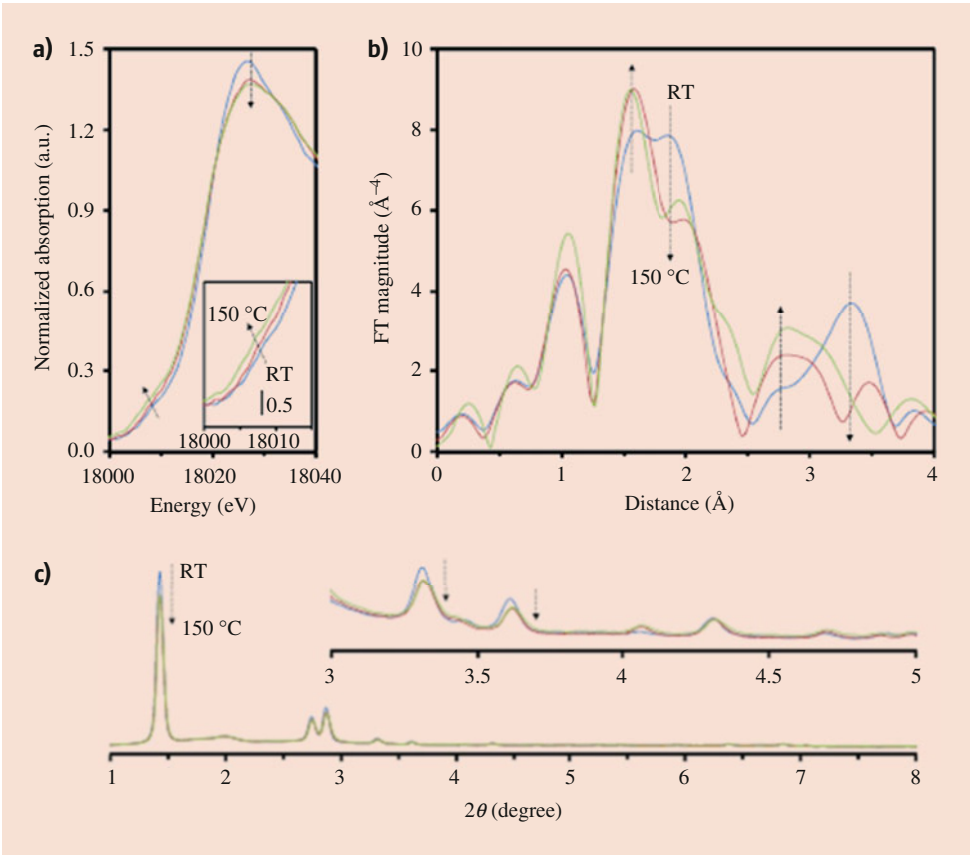

Fig. 33.11 XAS and XRD results during the thermal treatment. (**a**) Zr K-edge normalized XANES spectra, (**b**) Fourier transforms (FT) of k^3-weighted EXAFS of Zr-BTC, and (**c**) XRD patterns of the Zr-BTC/NaCl pellet measured at three different times during the thermal process and indicated in Fig. 33.12b (point 1, pattern blue; 2, red; and 3, green). (Reproduced from Ref. [18] with permission from John Wiley and Sons)

thermal treatment. Figure 33.12a corresponds to the ex situ IR spectrum of the Zr-BTC before the treatment and presents six broad bands in the characteristic frequency region. All these bands underwent intensity changes and/or position shifts as the temperature increased (Fig. 33.12b). During the thermal process, the desorption of water was mainly produced as evidenced by the sharp decrease of the broad feature around 3300 cm^{-1} characteristic of adsorbed H_2O with hydrogen bonding interactions.

The bands related to vibration modes of the acetate ligand on the Zr SBU thus are, at 1657 cm^{-1}, assigned to the asymmetric C-O stretching and, at ca. 1387 cm^{-1}, correspond to the combined C-C stretching and symmetric C-O stretching modes and underwent firstly slightly modifications (signal broadening or shift position) when water was extracted from the structure and then, around 150 °C (point 2, in Fig. 33.12b), more drastic changes with the disappearance of the bands. These results point to a higher stability of the acetate ligands than adsorbed water. Nevertheless, they can be gradually removed at 150 °C. Moreover, a small peak related to C-H bending vibration of acetate emerged at ca. 1480 cm^{-1} after water removal from the MOF structure and later disappeared concomitantly with the band at 1657 cm^{-1}. This implies that near the methyl group of the acetate ligand, the polarity environment changes during H_2O elimination.

The bands ascribed to BTC linker at 1450, 1571, and 1622 cm^{-1} showed only minor changes upon water removal; all bands red shifted due to stronger interactions between Zr-SBU and BTC after thermal treatment.

Therefore, IR data (Fig. 33.12) indicate that after removal of water within the pores, the acetate ligands were also extracted, causing modifications of the SBU structure. This is also supported by the XAS results (Fig. 33.11a, b) showing that the extraction of acetate linkers shortens the atomic distance between Zr cations causing a rearrangement of Zr coordination environment. In addition, XAS data indicate higher Zr electron density in these clustering units, caused by the absence of coordinating oxygen from the acetate linkers.

Drawing conclusions with such a detailed degree is only possible by combining multiple techniques in one setup, which allows a better understanding of the catalytic problem, especially by adding IR spectroscopy which can yield highly relevant chemical information to the electronic and structural insights provided by XAS. The combined data show that a targeted heat treatment allows modulating the electronic properties of the Zr centers, offering the possibility of obtaining different catalytic sites for distinct reactions; for example, the inert atmosphere treatment at 150 °C for a long enough time produces richer electronically Zr centers. This information is crucial to understand the functionality of the materials and to design new possible applications.

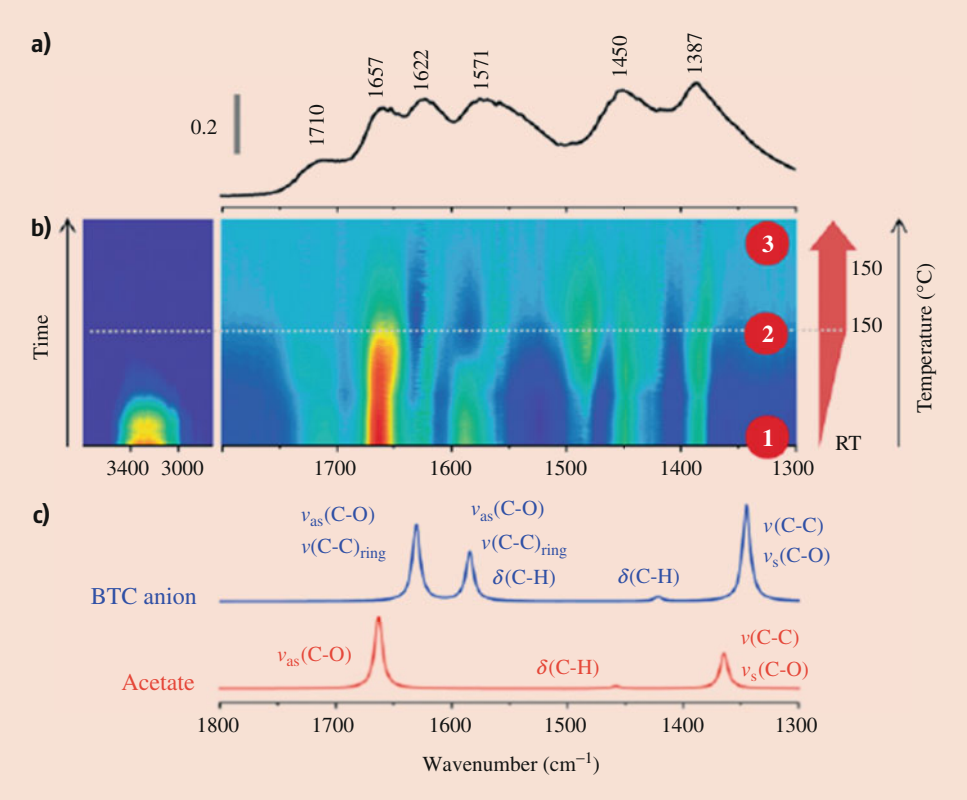

Fig. 33.12 (**a**) Ex situ transmission IR spectrum of Zr-BTC in air after the activation treatment. (**b**) Intensity color maps of the in situ transmission IR spectra during the thermal treatment (heat ramp from RT to 150 °C at 0.5 °C/min and then kept for 4 h). The last spectrum (i.e., at the end of the thermal treatment) was used as background. (**c**) Calculated IR spectra of BTC and acetate anions at B3PW91/6-311++G(2d,2p) and the band assignments from the normal mode analysis. (Reproduced from Ref. [18] with permission from John Wiley and Sons)

33.3 Summary

From a more general point of view, these examples clearly reveal how the catalytic phenomena emerge from a fine balance of electronic, geometric, and surface properties. Knowing how to optimize all these characteristics is crucial in designing ever-increasing performance catalysts, and for this, the synchronous use of several complementary characterization techniques is essential. This methodology represents a considerable advance since it allows untangling the chemistry of catalytic materials, defining the mechanism of catalytic reactions, and identifying the active sites.

This type of configuration has reached a great progress, but they are still under continuous technological improved development to expand the capabilities of the setups: measurements under a higher pressure range but without assuming a higher dead volume ensuring performance of optimal kinetic studies, faster acquisitions times, and combination with more other techniques. In addition, these equipment have considerable dimensions in general, and therefore, they also require adaptation of the synchrotron beamlines, since large spaces adaptable to these configurations are needed.

The higher flux synchrotron sources and the employment of more powerful lasers improve the capabilities but, at the same time, generate beam damage problems, laser heating effects, etc. more quickly. The interaction of the radiation with the sample or its environment may modify the atomic structure, crystal structure, or chemical state but also other parameters such as sample temperature and sample environment (gases, liquids). This may affect the experimental observables and introduce artifacts. It is necessary to develop mitigation strategies and propose measures that address these problems. They may involve the sample preparation and conditions during measurements, time resolution in pump-probe experiments, improvements of the X-ray detection, and data treatment.

On another hand, it has to be realized that this type of experiments combining several techniques results in more and comprehensive information, but it also produces a huge amount of data, in particular, when space- and time-resolved considerations are added. This implies the need for a large amount of storage capacity, processing a large amount of data, and then establishing correct correlations.

Therefore, all this requires associated software development as well as analysis interfaces and methodologies to satisfy all these demands.

References

1. Guerrero-Pérez, M.O., Bañares, M.A.: Chem. Commun. **12**, 1292 (2002)
2. Rodriguez, J.A., Hanson, J.C., Chupas, P.J.: In-Situ Characterization of Heterogeneous Catalysts. John Wiley & Sons, Ltd, United States of America, 2013 (2013)
3. (a) Marchionni, V., Nachtegaal, M., Ferri, D.: ACS Catal. **10**, 4791–4804 (2020); (b) Iglesias-Juez, A., Kubacka, A., Fernandez-Garcia, M., Di Michiel, M., Newton, M.A.: J. Am. Chem. Soc. **133**, 4484–4489 (2011); (c) Newton, M.A., Di Michiel, M., Kubacka, A., Iglesias-Juez, A., Fernández-García, M.: Angew. Chem. Int. Ed. **51**, 2363–2367 (2012); (d) Castillejos-Lopez, E., Agostini, G., Di Michel, M., Iglesias-Juez, A., Bachiller-Baeza, B.: ACS Catal. **7**(1), 796–811 (2017); (e) Kroner, A.B., Newton, M.A., Tromp, M., Russell, A.E., Dent, A.J., Evans, J.: Catal. Struct. React. **3**(1–2), 13–23 (2017); (f) Passos, A.R., La Fontaine, C., Martins, L., Pulcinelli, S.H., Celso, V., Briois, V.: Cat. Sci. Technol. **8**(24), 6297–6301 (2018); (g) Sprenger, P., Stehle, M., Gaur, A., Gaenzler, A.M., Gashnikova, D., Kleist, W., Grunwaldt, J.D.: ACS Catal. **8**(7), 6462–6475 (2018); (h) Bentrup, U.: Chem. Soc. Rev. **39**(12), 4718–4730 (2010); (i) Vovchok, D., Guild, C.J., Llorca, J., Xu, W., Jafari, T., Tolouenia, P., Kriz, D., Waluyo, I., Palomino, R.M., Rodriguez, J.A., Suib, S.L., Senanayake, S.D.: Phys. Chem. Chem. Phys. **19**, 17708–17717 (2017)
4. Bordiga, S., Groppo, E., Agostini, G., van Bokhoven, J.A., Lamberti, C.: Chem. Rev. **113**, 1736–1850 (2013)
5. Couves, J.W., Thomas, J.M., Waller, D., Jones, R.H., Dent, J.A., Derbyshire, G.E., Greaves, G.N.: Nature. **354**, 465–468 (1991)
6. Clausen, B.S., Topsøe, H.: Catal. Today. **9**, 189–196 (1991)
7. Beale, A.M., van der Eerden, A.M.J., Kervinen, K., Newton, M.A., Weckhuysen, B.M.: Chem. Commun., 3015–3017 (2005)
8. Frenkel, A.L., Wang, Q., Marinkovic, N., Chen, J.G., Barrio, L., Si, R., Camara, A.L., Estrella, A.M., Rodriguez, J.A., Hanson, J.C.: J. Phys. Chem. C. **115**, 17884–17890 (2011)
9. Tinnemans, S.J., Mesu, J.G., Kervinen, K., Visser, T., Nijhuis, T.A., Beale, A.M., Keller, D.E., van der Eerden, A.M.J., Weckhuysen, B.M.: Catal. Today. **113**, 3–15 (2006)
10. (a) Mesu, J.G., van der Eerden, A.M.J., de Groot, F.M.F., Weckhysen, B.M.: J. Phys. Chem. B. **109**, 4042–4047 (2005); (b) O'Brien, M.G., Beale, A.M., Jacques, S.D.M., Weckhuysen, B.M.: Top. Catal. **52**, 1400–1409 (2009); (c) Mesu, J.G., Beale, A.M., de Groot, F.M.F., Weckhysen, B.M.: J. Phys. Chem. B. **110**, 17671–17677 (2006); (d) Tromp, M., Sietsma, J.R.A., Van Bokhoven, J.A., van Strijdonck, G.P.F., van Haaren, R.J., van der Eerden, A.M.J., van Leeuwen, P.W.N.M., Koningsberger, D.C.: Chem. Commun., 128–129 (2003); (e) Kongmark, C., Martis, V., Rubbens, A., Pirovano, C., Lofberg, A., Sankar, G., Bordes-Richard, E., Vannier, R.-N., Van Beek, W.: Chem. Commun., 4850–4852 (2009); (f) Chernyshev, A.V., Guda, A.A., Cannizzo, A., Soloveva, E.V., Voloshin, N.A., Rusalev, Y., Shapovalov, V.V., Smolentsev, G., Soldatov, A.V., Metelitsa, A.V.: J. Phys. Chem. B. **123**, 1324–1331 (2019); (g) Luo, K., Roberts, M.R., Hao, R., Guerrini, N., Pickup, D.M., Liu, Y.-S., Edstrom, K., Guo, J., Chadwick, A.V., Duda, L.C., Peter, G.B.: Nat. Chem. **8**(7), 684–691 (2016); (h) Passos, A.R., Pulcinelli, S.H., Santilli, C.V., Briois, V.: Catal. Today. **336**, 122–130 (2019)
11. Newton, M.A., van Beek, W.: Chem. Soc. Rev. **39**, 4845–4863 (2010)
12. Newton, M.A., Jyoti, B., Dent, A.J., Fiddy, S.G., Evans, J.: Chem. Commun., 2382–2383 (2004)
13. Cavers, M., Davidson, J.M., Harkness, I.R., Rees, L.V.C., McDougall, G.S.: J. Catal. **188**, 426–430 (1999)
14. (a) Newton, M.A.: Top. Catal. **52**, 1410–1424 (2009); (b) Marinkovic, N.S., Wang, Q., Frenkel, A.I.: J. Synchrotron Rad. **18**, 447–455 (2011); (c) Beyer, K.A., Zhao, H., Borkiewicz, O.J., Newton, M.A., Chupas, P.J., Chapman, K.W.: J. Appl. Crystallogr. **47**, 95–101 (2014); (d) Yao, S., Mudiyanselage, K., Xu, W., Johnston-Peck, A.C., Hanson, J.C., Wu, T., Stacchiola, D., Rodriguez, J.A., Zhao, H., Beyer, K.A., Chapman, K.W., Chupas, P.J., Martinez-Arias, A., Si, R., Bolin, T.B., Liu, W., Senanayake, S.D.: ACS Catal. **4**, 1650–1661 (2014)

15. (a) Bando, K.K., Wada, T., Miyamoto, T., Miyazaki, K., Takakusagi, S., Gott, T., Yamaguchi, A., Nomura, M., Oyama, S.T., Asakura, K.: J. Phys. Conf. Ser. **190**, 012158 (2009); (b) Bando, K.K., Wada, T., Miyamoto, T., Miyazaki, K., Takakusagi, S., Koike, Y., Inada, Y., Nomura, M., Yamaguchi, A., Gott, T., Oyama, S.T., Asakura, K.: J. Catal. **286**, 165–171 (2012); (c) Chiarello, G.L., Nachtegaal, M., Marchionni, V., Quaroni, L., Ferri, D.: Rev. Sci. Instrum. **85**, 074102 (2014); (d) Marchionni, V., Kambolis, A., Nachtegaal, M., Krocher, O., Ferri, D.: Catal. Struct. React. **3**, 71–78 (2017)
16. Agostini, G., Meira, D., Monte, M., Vitoux, H., Iglesias-Juez, A., Fernandez-Garcıa, M., Mathon, O., Meunier, F., Berruyer, G., Perrin, F., Pasternak, S., Mairs, T., Pascarelli, S., Gorges, B.: J. Synchrotron Radiat. **25**, 1745–1752 (2018)
17. Meira, D.M., Monte, M., Fernandez-Garcıa, M., Meunier, F., Mathon, O., Pascarelli, S., Agostini, G.: J. Synchrotron Radiat. **26**, 801–810 (2019)
18. Hinokuma, S., Wiker, G., Suganuma, T., Bansode, A., Stoian, D., Huertas, S.C., Molina, S., Shafir, A., Rønning, M., van Beek, W., Urakawa, A.: Eur. J. Inorg. Chem. **2018**, 1847–1853 (2018)
19. (a) Wang, L.-L., Johnson, D.D.: J. Am. Chem. Soc. **129**, 3658–3664 (2007); (b) Mager-Maury, C., Bonnard, G., Chizallet, C., Sautet, P., Raybaud, P.: ChemCatChem. **3**, 200–207 (2011); (c) Oudenhuijzen, M.K., Van Bokhoven, J.A., Miller, J.T., Ramaker, D.E., Koningsberger, D.C.: J. Am. Chem. Soc. **127**, 1530–1540 (2005)
20. (a) Andrews, L., Wang, X., Manceron, L.J.: Chem. Phys. **114**, 1559–1566 (2001); (b) Mueller, W.M., Blackledge, J.P., Libowitz, G.G.: Metal Hydrides. Academic Press, New York and London, (1968)
21. Carosso, M., Vottero, E., Lazzarini, A., Morandi, S., Manzoli, M., Lomachenko, K.A., Jimenez Ruiz, M., Pellegrini, R., Lamberti, C., Piovano, A., Groppo, E.: ACS Catal. **9**, 7124–7136 (2019)
22. (a) Bus, E., van Bokhoven, J.A.: Phys. Chem. Chem. Phys. **9**, 2894–2902 (2007); (b) Vaarkamp, M., Miller, J.T., Modica, F.S., Koningsberger, D.C.: J. Catal. **163**, 294–305 (1996); (c) Reifsnyder, S.N., Otten, M.M., Sayers, D.E., Lamb, H.H.: J. Phys. Chem. B. **101**, 4972–4977 (1997); (d) Kubota, T., Sakura, K.A., Ichikuni, N., Iwasawa, Y.: Chem. Phys. Lett. **256**, 445–448 (1996); (e) Watari, N., Ohnishi, S.: J. Chem. Phys. **106**, 7531–7540 (1997)
23. Mager-Maury, C., Bonnard, G., Chizallet, C., Sautet, P., Raybaud, P.: ChemCatChem. **3**, 200–207 (2011)
24. (a) Biffis, A., Centomo, P., Del Zotto, A., Zecca, M.: Chem. Rev. **118**(4), 2249–2295 (2018); (b) Dhyani, V., Bhaskar, T.: Renew. Energy. **129**, 695–716 (2018); (c) Wang, J., Chen, H., Hu, Z., Yao, M., Li, Y.: Catal. Rev. Sci. Eng. **57**(1), 79–144 (2015)
25. (a) Iglesias-Juez, A., Kubacka, A., Fernandez-García, M., Di Michiel, M., Newton, M.A.: J. Am. Chem. Soc. **133**, 4484–4489 (2011); (b) Kubacka, A., Martínez-Arias, A., Fernández-García, M., Di Michiel, M., Newton, M.A.: J. Catal. **270**, 275–284 (2010)
26. Iglesias-Juez, A., Martínez-Arias, A., Newton, M.A., Fiddy, S.G., FernándezGarcía, M.: Chem. Commun., 4092–4094 (2005)
27. (a) Hendriken, B.L.H., Bobaru, S.C., Frenken, J.W.M.: Top. Catal. **36**, 43–54 (2005); (b) Hendriken, B.L.H., Ackermann, M.D., van Rijn, R., Stolz, D., Popa, I., Balmes, O., Resta, A., Werneille, D., Felici, R., Ferrer, S., Frenken, J.W.M.: Nat. Chem. **2**, 730–734 (2010); (c) van Rijn, R., Balmes, O., Felici, R., Gustafson, J., Wermeille, D., Westerton, R., Lundgren, E., Frenken, J.W.M.: J. Phys. Chem. C. **114**, 6875–6876 (2010)
28. (a) Gao, F., Wang, Y., Goodman, D.W.: J. Phys. Chem. C. **113**, 174–181 (2009); (b) Gao, F., Cai, Y., Gath, K.K., Wang, Y., Chen, M.S., Guo, Q.L., Goodman, D.W.: J. Phys. Chem. C. **113**, 182–192 (2009); (c) McClure, J., Goodman, D.W.: Chem. Phys. Lett. **469**, 1–13 (2009)
29. Jentys, A.: Phys. Chem. Chem. Phys. **1**, 4059–4063 (1999)
30. Maciejewski, M., Baiker, A.: Pure&Appl. Chem. **67**(11), 1879–1884 (1995)
31. Griffin, S.L., Champness, N.R.: Coord. Chem. Rev. **414**, 213295 (2020)
32. Bavykina, A., Kolobov, N., Khan, I.S., Bau, J.A., Ramirez, A., Gascon, J.: Chem. Rev. **120**(16), 8468–8535 (2020)
33. Furukawa, H., Gándara, F., Zhang, Y., Jiang, J., Queen, W.L., Hudson, M.R., Yaghi, O.M.: J. Am. Chem. Soc. **136**, 4369–4381 (2014)
34. Winarta, J., Shan, B., Mcintyre, S.M., Ye, L., Wang, C., Liu, J., Mu, B.: Cryst. Growth Des. **20**(2), 1347–1362 (2020)
35. Valenzano, L., Civalleri, B., Chavan, S., Bordiga, S., Nilsen, M.H., Jakobsen, S., Lillerud, K.P., Lamberti, C.: Chem. Mater. **23**, 1700–1718 (2011)
36. (a) Cavka, J.H., Jakobsen, S., Olsbye, U., Guillou, N., Lamberti, C., Bordiga, S., Lillerud, K.P.: J. Am. Chem. Soc. **130**, 13850–13851 (2008); (b) Bordiga, S., Bonino, F., Lillerud, K.P., Lamberti, C.: Chem. Soc. Rev. **39**, 4885 (2010); (c) Ji, P., Solomon, J.B., Lin, Z., Johnson, A., Jordan, R.F., Lin, W.: J. Am. Chem. Soc. **139**, 11325–11328 (2017); (d) Plonka, A.M., Wang, Q., Gordon, W.O., Balboa, A., Troya, D., Guo, W., Sharp, C.H., Senanayake, S.D., Morris, J.R., Hill, C.L., Frenkel, A.I.: J. Am. Chem. Soc. **139**, 599–602 (2017); (e) Hennig, C., Weiss, S., Kraus, W., Kretzschmar, J., Scheinost, A.C.: Inorg. Chem. **56**, 2473–2480 (2017)

Giovanni Agostini received his PhD at the University of Torino (Italy). He worked as beamline scientist at BM23/ID24 beamlines (ESRF, France) and as Senior Scientist at LIKAT Institute (Rostock, Germany). Currently, he is beamline responsible of NOTOS at synchrotron ALBA (Spain). His main research activity consists of the structural and electronic characterization of nanostructured materials by XAS combined by complementary techniques.

Ana Iglesias-Juez received her PhD at Universidad Autónoma de Madrid (Spain). She worked as Junior Scientist at Utrecht University (Netherlands), and currently, she is Tenured Scientist at the Institute of Catalysis and Petrochemistry (ICP-CSIC, Spain). She leads the group of "Heterogeneous Catalysis and Advanced Characterization Techniques." Her research activity includes catalyst in situ characterization by synchrotron radiation-based techniques and FTIR, UV-vis, and Raman.